IEEE Access
Multidisciplinary ⋮ Rapid Review ⋮ Open Access Journal

Received 18 August 2023, accepted 20 September 2023, date of publication 25 September 2023,
date of current version 28 September 2023.

Digital Object Identifier 10.1109/ACCESS.2023.3318598

RESEARCH ARTICLE

Analysis of Deloaded Wind Power in Hybrid AC/HVDC Systems by Frequency Stability Constrained Optimal Power Flow

SANGWON KIM[1], **(Member, IEEE)**
Department of Electrical Engineering, University of Ulsan, Ulsan 44610, South Korea
e-mail: angwon22@ulsan.ac.kr

This work was supported by the 2022 Research Fund of University of Ulsan under Grant 2022-0498.

ABSTRACT This paper investigates the relationship between the frequency support by voltage-source converter based high-voltage direct current (VSC-HVDC) systems and the deloaded wind power operation considering the frequency stability constraints. The frequency stability is incorporated as additional constraints in the optimal power flow (OPF) analysis. The reserve capacity of the wind power plants should be provided for frequency support, which requires wind power output suppression during the steady-state. On the contrary, this wind output curtailment is unnecessary if the frequency stability constraints can be satisfied by the fast frequency controller of the VSC-HVDC system. The optimal wind power deload ratio can be determined by the OPF calculation. A hybrid AC/VSC-HVDC system model is designed based on the IEEE 39-bus system. The inertia emulation control (IEC) method is applied to the slack converter for the primary frequency support. Sensitivity analysis on the frequency stability constraints, and the capacities of wind power plants and HVDC systems are carried out. It is validated that the primary frequency support of VSC-HVDC systems can reduce the wind power output suppression.

INDEX TERMS Deloaded wind power, frequency stability constraint, HVDC, inertia emulation control, optimal power flow, primary frequency support.

I. INTRODUCTION

A. BACKGROUND AND MOTIVATION

With the aim of developing more sustainable electric power systems, the share of renewable energy sources (RES), such as wind and solar generation, is increasing globally. In this context, voltage-source converter based high-voltage direct current (VSC-HVDC) systems have been evaluated as effective approaches for the RES integrations [1], [2], [3]. Unlike conventional line-commutated HVDC systems, which require significant reactive power consumption for commutation, the active and reactive power outputs of VSC-HVDC systems can be controlled independently [4], [5]. Owing to this benefit, VSC-HVDC systems can be installed in AC grids with high AC voltage variations and unpredictable wind output fluctuations [6].

The associate editor coordinating the review of this manuscript and approving it for publication was Pratyasa Bhui.

However, power-electronics-interfaced nonsynchronous wind power plants (WPPs) and VSC-HVDC systems do not provide inertia to AC grids [7]. This inertia reduction is a significant issue since the frequency deviation and rate of change of frequency (ROCOF) can be increased [8]. For instance, the increased frequency deviations after the output fluctuation of WPPs can trigger generator trip and load-shedding events [9], [10]. In order to cope with this problem, fast primary frequency regulations by VSC-HVDC systems have been proposed in previous studies.

Similarly, WPPs can participate in AC grid frequency support. The deloaded operation of WPPs is necessary to acquire reserve capacity. This deloaded operation leads to operation cost increments due to reduced wind power production. Meanwhile, deloaded wind power production is not necessary if the AC grid frequency does not violate the operation constraint. Hence, deloaded production can be avoided when AC frequency is supported by a VSC-HVDC system.

This work is licensed under a Creative Commons Attribution-NonCommercial-NoDerivatives 4.0 License.
For more information, see https://creativecommons.org/licenses/by-nc-nd/4.0/

In this context, the relationship among the system frequency constraints, curtailed wind output, and the controllability of a VSC-HVDC system should be discussed.

B. LITERATURE REVIEW

Previous studies [7], [11], [12] have focused on improving the frequency stability of power system models using multi-terminal VSC-HVDC systems. The frequency regulations by offshore WPPs are investigated in [13], [14], [15], and [16]. Frequency support by DFIG-type wind turbines is discussed in [17]. The frequency regulation through the coordination of wind turbines and synchronous generators is developed in [18]. The inertial response of wind turbines to improve the secondary frequency response is evaluated [19]. The adjustable frequency control of WPPs fed by multi-terminal HVDC grids is studied in [20]. Hybrid control strategies based on DC grid capacitors of VSC-HVDC systems and the kinetic energy of WPPs are proposed to improve the power system inertia responses in [21] and [22].

In particular, grid-forming-based converter control strategies have attracted significant attention for the frequency regulation. The controllers mimic the dynamic behaviors of synchronous generators. For example, the grid-forming-based converter can imitate the swing equation of a synchronous generator. This can be implemented in conventional AC grids with high compatibility. The effects of grid-forming converter placements on the primary frequency responses and small-signal stability are studied in [23] and [24] respectively. Dynamic performance improvements of WPPs by grid-forming-controlled battery energy storage systems are proposed in [25]. In a micro-grid system model, it is revealed in [26] that decentralized grid-forming converters are effective for system voltage control. The capabilities of low-frequency oscillation damping by VSC-HVDC systems are explained in [27] and [28]. The grid-forming control of a VSC-HVDC system feeding AC grids with low short-circuit ratios is discussed in [29].

One of the popular grid-forming controller methods is inertia emulation control (IEC), which mimics the inertial characteristics of synchronous generators [30], [31], [32], [33], [34], [35]. Based on an energy-storage system, a converter controller is designed to provide additional virtual inertia during a short-term period. Consequently, the frequency response of an AC grid can be improved due to the increased system inertia. The impacts of HVDC systems with the IEC on the primary frequency regulations are analyzed in [11], [11], and [36]. The effect of IEC utilizing the electrostatic energy stored in DC-link capacitors is emphasized in [11]. It is demonstrated in [11] that IEC can be applied to multi-terminal VSC-HVDC systems. Frequency regulation by the IEC with adjustable emulated inertia is developed in [36].

Although these previous studies have accomplished notable outcomes for the primary frequency regulations, the following limitations remains.

1) The influence of the frequency support by a VSC-HVDC system on the reserve capacity of WPPs has not yet been analyzed. Previous studies have only focused on the frequency support of either WPPs or a VSC-HVDC system separately. However, WPPs have been integrated into power systems via VSC-HVDC systems in many projects. Therefore, the frequency stability analysis considering the frequency control of both WPPs and VSC-HVDC systems is essential.
2) The formulation for such an analysis has not been developed. Optimal power flow (OPF) analysis is an effective approach for determining the power system operations while satisfying feasible constraints. It is discussed in [38] that the frequency stability of a power system model can be handled as additional constraints in the OPF analysis. The frequency stability constrained OPF considering the dynamics of governor systems is studied in [47]. Nevertheless, the OPF analysis with frequency stability constraints considering the frequency support of both WPPs and VSC-HVDC systems is not found.

C. CONTRIBUTION IN THIS PAPER

In order to cover these limitations, the frequency constraints, the frequency control effects of a VSC-HVDC system, and the amount of WPPs curtailment should be formulated in an integrated OPF analysis. This can be adopted by power system operators to determine the optimal amount of wind output suppression minimizing the system operation cost. Compared to previous works, the main contributions of this paper are summarized as follows:

1) The frequency stability constrained-optimal power flow (FSC-OPF) model that schedules the active power outputs and reserve capacities of generators, WPPs, and HVDC systems is formulated. The power outputs and reserve capacities which minimize the generators' operation costs are determined. The frequency stability of a hybrid AC/HVDC model is handled as additional constraints in the OPF analysis.
2) The benefit of the HVDC frequency support is investigated from the perspective of wind output curtailment. The deloaded operation of WPPs results in increased power production of generators. This is undesirable for the minimization of the system operation cost. Nevertheless, the deloaded wind operation is required to offer additional reserve capacity when the frequency support by HVDC systems is not effective in satisfying the frequency constraints. On the other hand, the wind power output curtailment is unnecessary if the frequency can be well-controlled by the HVDC system.
3) The proposed FSC-OPF method is applied to the sensitivity analysis of the wind deload ratio. The influences of the frequency stability constraints, the capacities of HVDC systems, and WPPs on the wind deload ratio are discussed.

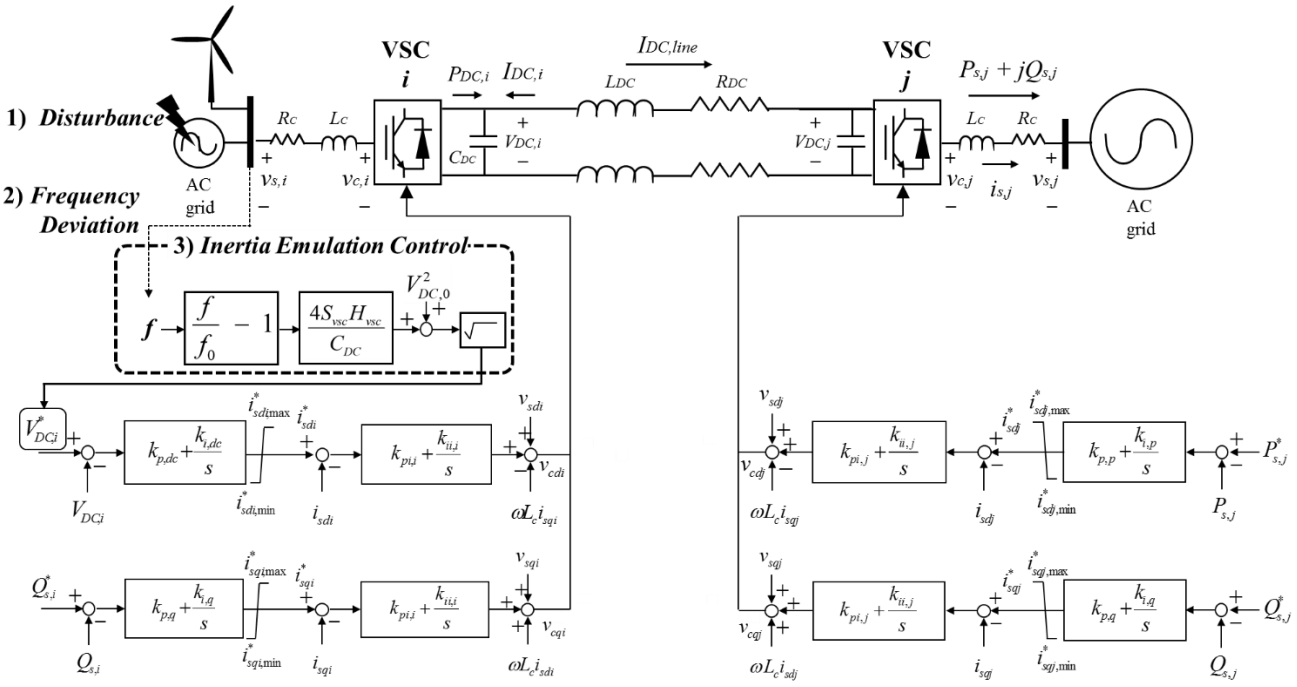

FIGURE 1. Average value model of a point-to-point VSC-HVDC system.

The remainder of this article is organized as follows. The VSC-HVDC system model with a frequency controller is described in Section II. Section III illustrates the WPP model with deloaded operation. The FSC-OPF analysis is presented in Section IV. A hybrid AC/HVDC power system model is explained in Section V. The numerical results are discussed in Section VI.

II. VSC-HVDC SYSTEM MODEL

A. AVERAGE VALUE MODEL

Modular multi-level converter (MMC) HVDC systems have been installed in many large-scale VSC-HVDC systems recently. The most accurate MMC HVDC model considers the individual behaviors of all sub-modules which yields a high computational process. On the contrary, detailed sub-module behaviors can be neglected in the average value model (AVM). The AVM model can be adopted for dynamic behavior analysis with reduced calculation burden and reasonable accuracy [39], [40].

The average value model of a point-to-point VSC-HVDC system is described in FIGURE 1. Each bus number is denoted by the letters '*i*' or '*j*'. The slack converter VSC *i* is in charge of controlling the DC bus voltage. VSC *j* controls the active power output. In addition, each VSC converter can control the reactive power output.

The hybrid AC/VSC-HVDC system is interconnected via point of common coupling (PCC) buses. R_c and L_c correspond to the AC transformers and filters of these interconnections. The angular frequency of the AC grid is denoted as ω.

Equations (1) and (2) represent the voltage relationships between v_s and v_c in the synchronously rotating *dq* axis. The outputs of the vector current outer controllers are notated in i_{sd} and i_{sq}. Kirchhoff's current law at DC bus *i* is given by (3). For example, $V_{DC,i}$ and $C_{DC,i}$ correspond to the DC bus voltage and capacitance, respectively. The active power and current injected at DC bus *i* are represented by $P_{DC,i}$ and $I_{DC,i}$. $I_{DC,line}$ means the DC current flow between DC buses *i* and *j*. Thus, equation (4) determines the DC transmission line current flow. The active and reactive power outputs of the VSC converter at bus *i* can be denoted as $P_{s,i}$ and $Q_{s,i}$ in (5) and (6), respectively.

$$L_c \frac{di_{sdi}}{dt} = -R_c i_{sdi} + \omega L_c i_{sqi} + v_{cdi} - v_{sdi} \quad (1)$$

$$L_c \frac{di_{sqi}}{dt} = -R_c i_{sqi} - \omega L_c i_{sdi} + v_{cqi} - v_{sqi} \quad (2)$$

$$C_{DC} \frac{dV_{DC,i}}{dt} = -\frac{P_{DC,i}}{V_{DC,i}} + I_{DC,i} \quad (3)$$

$$L_{DC} \frac{dI_{DC,line}}{dt} = -R_{DC} I_{DC,line} + V_{DC,i} - V_{DC,j} \quad (4)$$

$$P_{s,i} = v_{sdi} i_{sdi} + v_{sqi} i_{sqi} \quad (5)$$

$$Q_{s,i} = v_{sqi} i_{sdi} - v_{sdi} i_{sqi} \quad (6)$$

B. INERTIA EMULATION CONTROL

As regards the primary frequency control of the VSC-HVDC system, the inertia emulation control (IEC) in [11] and [36] is implemented in the VSC slack in FIGURE 1. The DC voltage reference V_{DC_ref} can be adjusted by the IEC. The inertial behavior of the synchronous generators is reflected in the V_{DC_ref} adjustment.

The inertia constant of a synchronous generator H is defined in (7), which is the ratio of the rotational kinetic energy to the generator machine rating S_G. J represents the moment of inertia. The subscript *0* indicates the steady-state, thus, the angular rotational speed of the generator is notated in ω_0.

In the IEC, the inertia constant of the slack VSC, H_{vsc} can be defined in a similar way in (8). The numerator indicates the electromagnetic energy of the DC grid capacitor C_{DC}. The VSC converter rating is notated in S_{vsc}.

$$H = \frac{\frac{1}{2}J\omega_0^2}{S_G} \tag{7}$$

$$H_{vsc} = \frac{\frac{1}{2}C_{DC}V_{DC,0}^2}{S_{VSC}} \tag{8}$$

The transient rotational characteristics of the synchronous generator are described by (9). The mechanical power input and electrical power output are represented by P_m and P_e respectively. f stands for the AC grid system frequency. S indicates the power rating of the synchronous generator. Based on the approximation $f \approx f_0$ in the per-unit system, equation (9) can be simplified in (10).

$$\frac{2HS}{f_0^2} f \frac{df}{dt} = P_m - P_e \quad [\text{MW}] \tag{9}$$

$$\frac{2H}{f_0} \frac{df}{dt} = P_m - P_e \quad [p.u.] \tag{10}$$

The underlying principle of the IEC can be introduced based on the analogy between the behavior of synchronous generators and VSC converters. The notations H and f of the generators can be replaced by the inertia constant H_{vsc} and the DC bus voltage V_{DC} of the VSC slack converter. As a consequence, the following relationship in (11) can be obtained. P_{in} and P_{out} in (11) represent the active power input and output values of the VSC slack converter respectively.

$$\frac{C_{DC}V_{DC}}{S_{vsc}} \frac{dV_{DC}}{dt} = P_{in} - P_{out} \quad [p.u.] \tag{11}$$

Based on (10) and (11), the relationship in (12) can be defined from the perspective of active power flow. By integrating both sides of (12), equations (13) and (14) can be derived. The DC bus voltage controller of the IEC can be defined in (15) by letting $V_{DC\_ref} = V_{DC}$.

The definition of the IEC in (15) shows that the DC voltage reference value $V_{DC,ref}$ $(= V_{DC}^*)$ of the VSC slack converter can be adjusted by the AC grid frequency deviation ratio f/f_0. If an AC grid frequency drop is detected, V_{DC_ref} reference value decreases to release the active power into the AC grid.

$$\frac{2H_{vsc}}{f_0} \frac{df}{dt} = \frac{C_{DC}V_{DC}}{S_{vsc}} \frac{dV_{DC}}{dt} \tag{12}$$

$$\int_{f_0}^{f} \frac{2H_{vsc}}{f_0} df = \int_{V_{DC,0}}^{V_{DC}} \frac{C_{DC}V_{DC}}{S_{vsc}} dV_{DC} \tag{13}$$

$$\frac{2H_{vsc}}{f_0}(f - f_0) = \frac{C_{DC}}{2S_{vsc}}(V_{DC}^2 - V_{DC,0}^2) \tag{14}$$

$$V_{DC,ref} = \sqrt{V_{DC,0}^2 + \frac{4S_{vsc}H_{vsc}}{C_{DC}}(\frac{f}{f_0} - 1)} \tag{15}$$

III. WIND POWER PLANT MODEL WITH DELOADING CONTROL

A. WIND POWER PLANT MODEL

The aggregated wind power plant model is depicted in FIGURE 2. The wind turbine is connected to the AC grid via the rotor-side and grid-side converters. The dynamic behavior of these converters is typically very fast. Therefore, it is assumed that the active power output of the wind turbine P_{WT} can follow the reference value without delay [20].

The VSC technology is widely applied to the rotor-side and grid-side converters. Not only the active power, this VSC type converter can also regulate the reactive power output. For the simplicity, the contribution of active power output is simulated while the reactive power regulation is neglected in this paper. The dynamic behaviors by the reactive power controllability will be discussed in the future.

The rotational behavior of the wind turbine can be represented as (16)-(17). The inertia constant of the wind turbine is notated in H_{WT}. ω_r is the rotor speed of the wind turbine. $P_{m,WT}$ corresponds to the mechanical power input value which is equal to the steady-state wind power output.

$$2H_{WT}\omega_r \frac{d\omega_r}{dt} = P_{m,WT} - P_{WT} \quad [p.u.] \tag{16}$$

$$\frac{d\omega_r}{dt} = \frac{1}{2H_{WT}\omega_r}(P_{m,WT} - P_{WT} \quad)[p.u.] \tag{17}$$

The active power output of the wind model is determined by the maximum power point tracking (MPPT) controller (18). The coefficient C_{WT} depends on the blade radius, the air density, and the ratio of the wind speed to the rotor speed. In addition, the AC grid frequency controller in (19) is implemented in the wind model. The controller measures the frequency f_{WF} and produces the active power adjustment P_f when a frequency deviation from the nominal frequency $f_{WF,0}$ is detected. The wind power output P_{WT} consists of the sum of P_{MPPT} and P_f in (20) – (21).

$$P_{MPPT} = C_{WT}\omega_r^3 \tag{18}$$

$$P_f = k_f(f_{WT,0} - f_{WT}) \tag{19}$$

$$P_{WT} = P_{MPPT} + P_f \tag{20}$$

$$P_{WT} = C_{WT}\omega_r^3 + k_f(f_{WF,0} - f_{WF}) \tag{21}$$

B. DELOADING CONTROL

Instead of maximum power point tracking, the deloading control of a wind turbine can be implemented to secure the reserve capacity for AC grid frequency control [41]. The major methods for the deloading control are rotor overspeed control and pitch-angle control [41], [42].

Compared to the rotational speed on the MPPT curve, the output of a wind turbine can be reduced by the rotor-speed adjustment. Both increasing and decreasing the speed can reduce the output. However, the decreased speed of operation

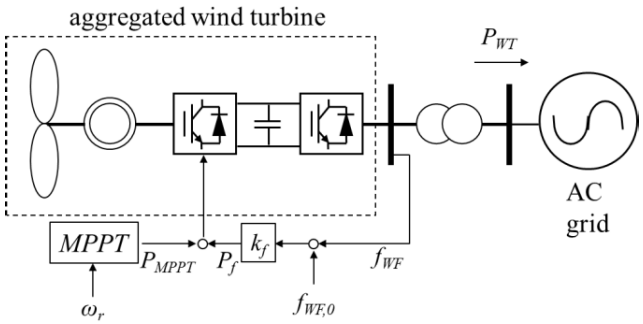

FIGURE 2. Wind power plant model with frequency support [20].

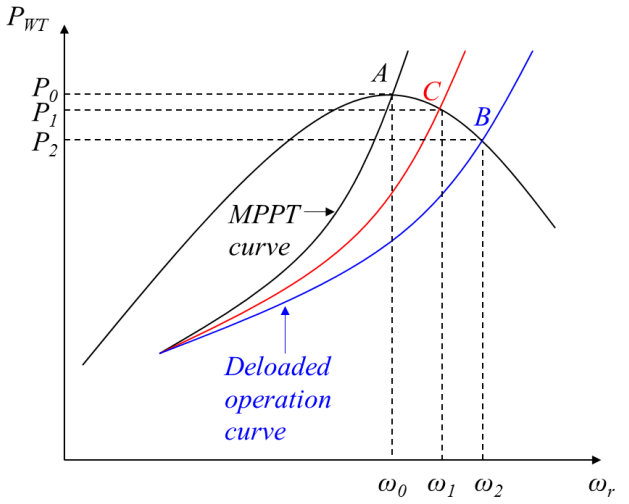

FIGURE 3. Overspeed method of WT for deloading control [41].

may result in a stability issue caused by a small interference. Hence, the overspeed rotor control method is adopted in general.

If the operation point for the maximum power output production is at point A in FIGURE 3, the wind turbine can be operated at the shifted point B. The active power output is reduced from P_0 to P_2 by adjusting the rotational speed from ω_0 to ω_2. When a frequency drop is observed, the speed decreases from ω_0 to ω_1 to increase the power output from P_2 to P_1 at point C.

The pitch angle of a wind turbine is maintained at zero during normal operation. On the contrary, the wind turbine can be operated in a deloaded state if the pitch angle increases. The angle decreases to support the AC grid frequency when a frequency drop is observed. Wind power output can be adjusted over a wide range by using this method. Nonetheless, the pitch angle control method is not feasible when the wind speed is slow. Furthermore, it is not suitable for fast response speed implementations due to the mechanical inertia behavior. Therefore, it is assumed that the overspeed control of a wind turbine is applied for the fast primary frequency control.

IV. OPTIMAL POWER FLOW WITH FREQUENCY STABILITY CONSTRAINT

A. OPTIMAL POWER FLOW FORMULATION

The OPF analysis of the hybrid AC/VSC-HVDC system with deloaded wind operation can be summarized in (22) – (25) as follows:

$$f_0(x_o, u_o) = \sum_{n \in G} (C_n + B_n P_n + A_n P_n^2) \tag{22}$$

$$g_o(x_o, u_o) = 0 \tag{23}$$

$$h_o(x_o, u_o) \leq 0 \tag{24}$$

$$h_k(x_k, u_k) \leq 0 \tag{25}$$

where the vectors of control and state variables are denoted by u and x respectively. The objective function (22) is defined as the total operation cost of all generators.

The operation cost of a generator n is the quadratic function of the active power output P_n. A_n, B_n, and C_n are the coefficients of the quadratic cost function. The equality g and inequality h constraints for the steady-state operation are represented in (23) and (24), respectively. The inequality constraint after the disturbance k is considered in (25).

Regarding the equality constraint (23), the balance of active and reactive power in the AC grid bus j_AC is included in (26) and (27). On top of that, the balance of the active power in the DC grid bus j_DC is considered for hybrid AC/HVDC systems in (28).

$$P_{n,j} - P_{load,j} + P_{vsc,j} = P_{j\_AC} \tag{26}$$

$$Q_{n,j} - Q_{load,j} + Q_{vsc,j} = Q_{j\_AC} \tag{27}$$

$$P_{n,DC,j} - P_{DC\_load,j} + P_{vsc,DC,j} = P_{j\_DC} \tag{28}$$

The inequality constraint in (24) contains the lower and upper limits of the power system steady-state operation. In (29) – (31), the active P, reactive Q, and apparent power S outputs of generator n are constrained. For hybrid AC/HVDC systems, the VSC power outputs should also be limited (32)–(34). The deviations of voltage magnitudes at all AC and DC buses below 0.9 *p.u.* or above 1.1 *p.u.* are not allowed in (35) and (36). In (37) and (38), the active power flow via a transmission line and tap transformer ratios should be operated within their respective ratings.

$$P_n^{\min} \leq P_n \leq P_n^{\max} \tag{29}$$

$$Q_n^{\min} \leq Q_n \leq Q_n^{\max} \tag{30}$$

$$S_n^{\min} \leq S_n \leq S_n^{\max} \tag{31}$$

$$P_{vsc}^{\min} \leq P_{vsc} \leq P_{vsc}^{\max} \tag{32}$$

$$Q_{vsc}^{\min} \leq Q_{vsc} \leq Q_{vsc}^{\max} \tag{33}$$

$$S_{vsc}^{\min} \leq S_{vsc} \leq S_{vsc}^{\max} \tag{34}$$

$$V_{AC}^{\min} \leq V_{AC} \leq V_{AC}^{\max} \tag{35}$$

$$V_{DC}^{\min} \leq V_{DC} \leq V_{DC}^{\max} \tag{36}$$

$$P_{line}^{\min} \leq P_{line} \leq P_{line}^{\max} \tag{37}$$

$$R_{Tap}^{\min} \leq R_{Tap} \leq R_{Tap}^{\max} \tag{38}$$

Not only the power balance in the AC and DC grids in (39)– (41), the frequency stability of the power system model is also analyzed after the disturbance k. The frequency of each generator f_n is monitored to avoid deviating above the frequency criterion range f_{range} in (42). Similarly, the fluctuation of the frequency at the center of inertia f_{COI} above f_{range} is also prohibited in (43) [43], [44].

A significant DC bus voltage fluctuation can occur when the IEC is activated. The DC bus voltage magnitude is maintained not to deviate below 0.9 *p.u.* or above 1.1 *p.u.* to prevent this phenomenon in (45).

$$P_{n,j,k} - P_{load,j,k} + P_{vsc,j,k} = P_{j\_AC,k} \tag{39}$$

$$Q_{n,j,k} - Q_{load,j,k} + Q_{vsc,j,k} = Q_{j\_AC,k} \tag{40}$$

$$P_{n,DC,j,k} - P_{DC\_load,j,k} + P_{vsc,DC,j,k} = P_{j\_DC,k} \tag{41}$$

$$f_n = f_{n,0} \pm f_{range} \quad n = 1, 2, \cdots, G \tag{42}$$

$$f_{COI,k} = f_{COI,0} \pm f_{range} \tag{43}$$

$$f_{COI} = \sum_{n \in G} \frac{f_n H_n}{H_n} \tag{44}$$

$$V_{DC,k}^{\min} \le V_{DC,k} \le V_{DC,k}^{\max} \tag{45}$$

In order to supply additional reserve capacity from the wind power side, wind power plants can be operated under deloaded conditions in the steady-state. However, the amount of the wind output curtailment should be determined carefully since the curtailment leads to an increased production of generators. As a result, the objective function value in (22) can be increased. In this paper, the deload ratio of wind power plants is determined by the FSC-OPF analysis.

The upper limit of the deload ratio R_{WT} is one, which means that there is no wind output curtailment. The lower limit of the ratio R_{WT} can be determined considering the performance of the wind turbine rotor-speed adjustment and pitch angle control. This can be incorporated as an inequality constraint in the steady-state operation in (24). During the optimization procedure, the deload ratio R_{WT} is optimized as one of the control variables u within the constraint (46).

$$R_{WT}^{\min} \le R_{WT} \le R_{WT}^{\max} \tag{46}$$

B. OPTIMIZATION ALGORITHM

Differential evolution is adopted as the optimization algorithm. Compared to conventional mathematical approaches such as interior point methods, dynamic power system stability constraints can be simply integrated into the OPF analysis as additional constraints by this metaheuristic-based method. Nevertheless, a large computational burden is required if the number of optimization parameters increases. In order to overcome this disadvantage, the optimization process can be revised by adding the filtering out process [37], [38] in FIGURE 4.

First of all, the control vector component values 'u' are initialized randomly within their respective minimum and maximum operational ranges. The parent control vector set '*u_set*' is composed of these control vector components.

The feasibility of each u vector should be checked. Power flow analysis is performed for each control vector u. The control vector is feasible if the constraints (23) – (41) are not violated. A large penalty value is added to the fitness function of an infeasible control vector.

As regards the dynamic stability constraints (42) – (45), the time-domain simulation is performed. However, it is inefficient from the viewpoint of computational time if the time-domain simulation is conducted for all control vectors. Instead, the stability constraints (42) – (45) are checked only for the feasible vectors [38]. The fitness function of a feasible vector is penalized by adding the penalty value 'α' when one of the constraints (42) – (45) is violated. The filtering penalty value 'β' is added to all other infeasible control vectors. For an effective filtering process, the penalty value α should be smaller than β.

The trial vector set '*w_set*' is produced after the mutation and crossover stages. Power flow analysis and the time-domain simulation with the filtering out are carried out for these trial vectors.

The fitness functions of u_n and w_n are compared to select a superior vector. A vector with a lower fitness function value is chosen to minimize the objective function value. The optimization process repeats the entire sequence for the maximum iteration number.

V. POWER SYSTEM MODEL

The power system model is described in FIGURE 5. The model is designed based on the IEEE 39-bus system. The operation cost coefficients of the generators in [45] are adopted. Loads in the AC grid are modeled as constant power models.

A wind farm is installed near generator G7. It is assumed that the wind farm can be deloaded by 0∼10% during the steady-state operation to secure the reserve capacity. For example, the steady-state power production of a 600MW wind farm can be suppressed by 60MW. This reserve capacity can be utilized to support the AC grid frequency when a frequency deviation occurs. The inertia constant of the wind turbine H_{WT} is 4 seconds.

As the disturbance type, a sudden switchable load addition near G7 is simulated. The active and reactive power consumptions of the switchable load are 500MW and 150MVAR respectively. Generators G1 ∼ G9 are equipped with the AVR and GOV models in the Appendix. The IEEE Type 1 excitation [46] and reheated steam turbine models [47] are adopted. The parameters of the AVR and GOV models are listed in Tables 4 and 5, respectively, in the Appendix.

The power system is reinforced by a 500kV point-to-point VSC-HVDC system. VSC 1 and VSC 2 control the DC voltage and active power output respectively. The IEC control is implemented in the slack converter VSC 1 for the primary frequency support. The DC bus voltage reference value of VSC 1 is 1.0 *p.u.* in the steady-state. After the disturbance, this reference can be adjusted by the IEC. The control system

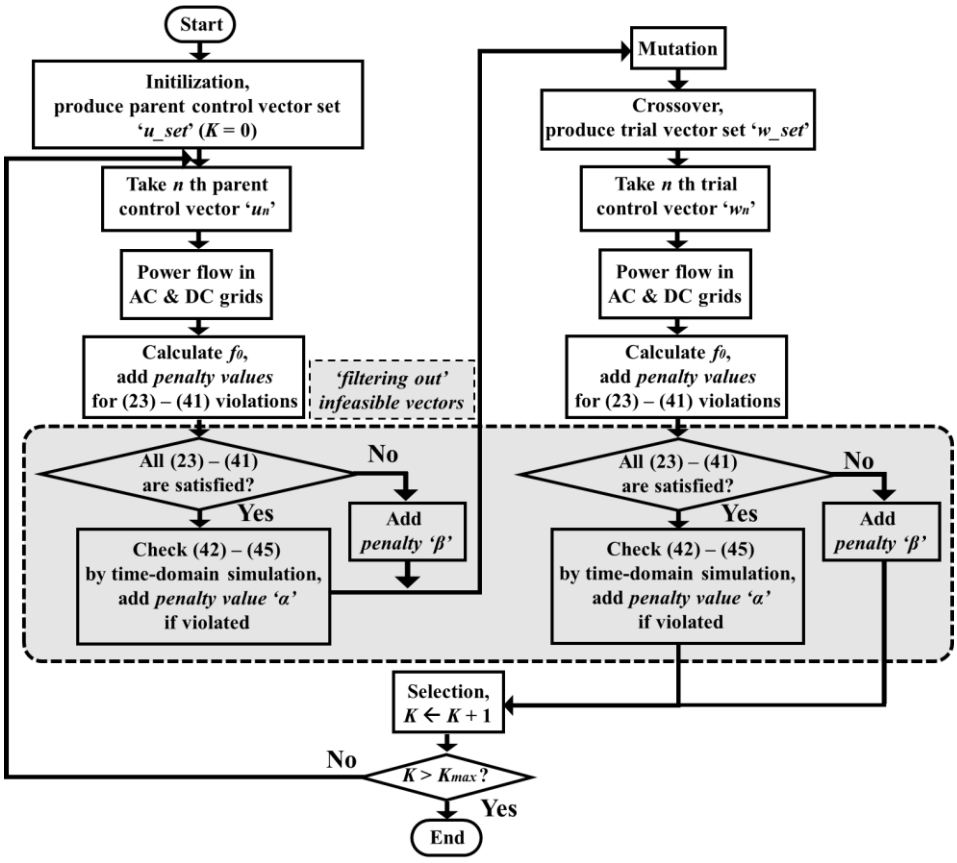

FIGURE 4. Algorithm of OPF with filtering out process [37], [38].

parameters of the VSC-HVDC system are tuned by a preliminary process, which are listed in Table 6, Appendix.

In order to obtain effective IEC performance by the VSC-HVDC system, the DC capacitor rating C_{DC} should be determined properly. If a large C_{DC} capacity is required, additional storage devices such as super-capacitors can be added. As a result, the installation cost of the VSC-HVDC system increases. A low rating of C_{DC} yields large deviations in DC bus voltages when the IEC is activated. Therefore, it is difficult to satisfy the DC bus voltage constraint with a low C_{DC} rating. Proper C_{DC} ratings for effective IEC implementations are discussed in [11], [36], and [48].

VI. SIMULATION RESULTS

A. TIME-DOMAIN SIMULATION RESULTS

Depending on the frequency constraints and system configurations, three cases are classified in the time-domain simulation analysis. In this section, H_{vsc} is zero in *Case 3*. The capacity of the VSC-HVDC system is 1000MVA in *Case* 3. The rated output of the wind power plant is 600MW with the unity power factor.

*Case*1 : *No HVDC*, $f_{range} = 0.15$Hz
*Case*2 : *No HVDC*, $f_{range} = 0.14$Hz
*Case*3 : *Hybrid AC/HVDC system*, $f_{range} = 0.115$Hz

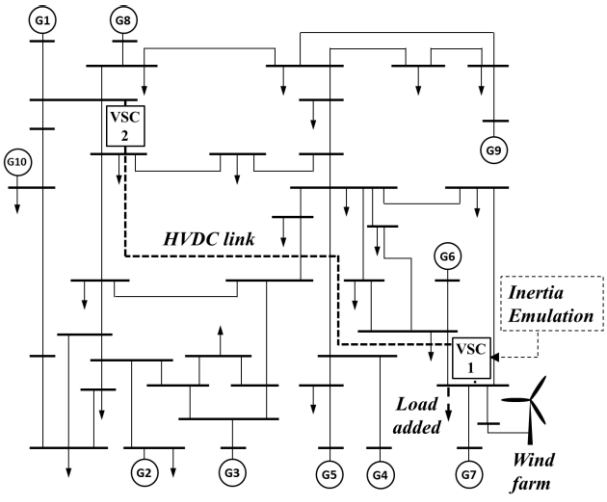

FIGURE 5. Modified IEEE 39-bus system model (Hybrid AC/HVDC).

A switchable load is added at $t = 1$ second. The rotational speed trajectories of generators G6 and G7 near the switchable load are plotted in FIGURE 6. The trajectories of G6 and G7 are drawn in black and blue lines respectively. The active power output curves of the wind farm are described in FIGURE 7.

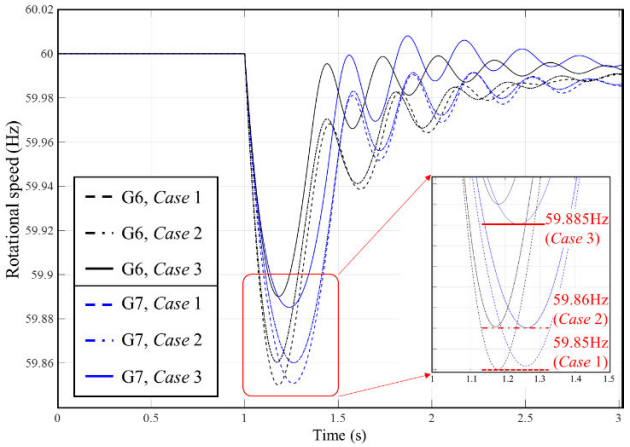

FIGURE 6. Rotational speed trajectories of generators G6 and G7.

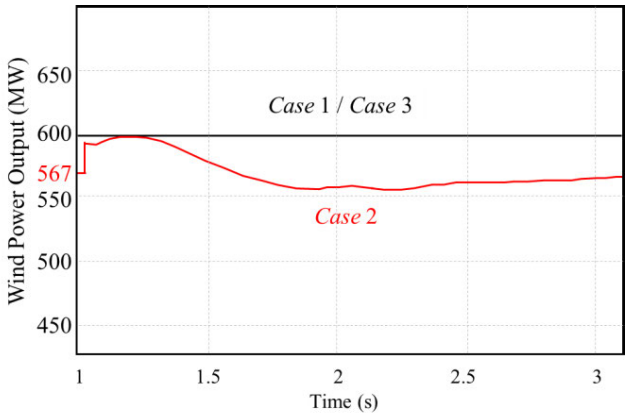

FIGURE 7. Active power output of wind power plant.

It can be seen in FIGURE 6 that the nadir values of G6 and G7 are 59.85Hz in *Case* 1. On the contrary, those values can be supported by 0.01Hz in *Case* 2 owing to the frequency support of the wind power plant. When a frequency drop at the PCC bus of the wind power plant is detected, the active power output of the wind power increases by 23MW for the frequency support in *Case* 2. To this end, the wind power plant is deloaded to guarantee the reserve capacity during the steady-state operation. The deload ratio R_{WT} of the wind power plant is 0.945 in FIGURE 7.

It should be noted that in *Case* 3, the wind power plant is not deloaded as shown in FIGURE 7. The same result can be obtained for $f_{range} = 0.15\text{Hz} \sim 0.115\text{Hz}$ in *Case* 3. This indicates that the deloaded operation of the wind power plant is not necessary owing to the fast frequency control of the HVDC system.

B. SENSITIVITY ANALYSIS ON FREQUENCY STABILITY CONSTRAINTS

The OPF formulation with different frequency stability constraints is carried out. The wind deload ratio R_{WT} of the power system models with and without the VSC-HVDC system is presented in Table 1. The notation 'X' indicates the OPF solution is not found, which means such scenarios are infeasible. As regards the hybrid AC/HVDC system, the capacity of the HVDC system is 1000MVA. The pre-disturbance active and reactive power output of the wind power plant is 600MW and zero respectively. Three cases with different H_{vsc} parameters are tested for the hybrid AC/HVDC system.

TABLE 1. Deload ratio of wind power plant R_{WT} with different frequency stability constraints.

f_{range}	No HVDC	Hybrid AC/HVDC		
		H_{vsc} (sec)		
		0	0.5	1
0.15Hz	1	1	1	1
0.14Hz	0.945	1	1	1
0.13Hz	0.945	1	1	1
0.12Hz	X	0.997	1	1
0.11Hz	X	0.949	0.988	1
0.10Hz	X	0.949	0.972	1
0.09Hz	X	X	0.972	0.980

When the frequency stability constraint f_{range} is 0.15Hz, the deloaded wind operation is not necessary for all cases. Without the HVDC system, the wind power plant output should be deloaded by 5.5% compared to the rated output of 600MW when the constraint f_{range} is both 0.14Hz and 0.13Hz. No feasible solution is found when the frequency constraint f_{range} is less than or equal to 0.12Hz.

On the contrary, the deloaded wind power operation is not required in the hybrid AC/HVDC system models for 0.14Hz or 0.13Hz frequency constraints. When H_{vsc} is zero, 0.3% wind power output curtailment is necessary if the constraint f_{range} is 0.12Hz. When the frequency constraint f_{range} is both 0.11Hz and 0.10Hz, the pre-fault wind power output should be suppressed by 5.1% to guarantee the reserve capacity. The feasible OPF solution cannot be obtained when the constraint f_{range} is less than or equal to 0.09Hz.

The primary frequency support can be provided by the IEC control when H_{vsc} is positive. Consequently, the wind-side-source does not have to secure the reserve capacity. As a result, the deload ratio R_{WT} can be reduced. When H_{vsc} is 0.5 seconds, the deloaded wind operation is not required for the 0.12Hz constraint f_{range}. Similarly, no wind power output suppression is needed for the case of 0.10Hz frequency constraint f_{range} when H_{vsc} is 1 second.

In summary, the system operation without the HVDC system is not feasible when the frequency constraint f_{range} is 0.12Hz. In contrast, feasible OPF solutions of the hybrid AC/HVDC system can be obtained if the deloaded wind operation is taken into account. The deloaded operation is not necessary if the IEC control is implemented for the primary frequency control. Therefore, the lowest deload ratio values can be obtained for the scenarios of all frequency stability constraints f_{range} when H_{vsc} is one.

TABLE 2. Deload ratio of wind power plant R_{WT} with different wind capacity.

Wind Capacity	No HVDC	Hybrid AC/HVDC	
		H_{vsc} (sec)	
		0	1
200MW	X	0.914	1
400MW	X	0.922	1
600MW	X	0.949	1

C. SENSITIVITY ANALYSIS ON WIND CAPACITY

Scenarios with three different wind power plant capacities are investigated. The deload ratio results R_{WT} of the wind model are listed in Table 2. In this section, the HVDC system capacity is 1000MVA. The frequency stability constraint f_{range} is 0.12Hz.

No feasible operation solution is calculated for the pure AC system model. This implies that the wind power plant cannot provide a sufficient reserve capacity to satisfy the frequency stability constraint in all three scenarios.

On the contrary, feasible solutions can be found in the hybrid AC/HVDC system models. When H_{vsc} is zero, the deload ratio results are not one. In other words, the pre-disturbance wind power plant outputs should be curtailed if the IEC control is not applied. In particular, the lowest ratio value is obtained when the wind power plant capacity is 200MW. Thus, it can be concluded that the amount of wind power output suppression decreases if the installed wind power plant capacity increases.

If H_{vsc} is 1 second, the deload ratio value is always one for all wind capacity scenarios. In this case, the frequency stability constraint can be satisfied by the frequency support of the HVDC system. Hence, the frequency control by the wind power plant is unnecessary regardless of the wind capacity.

D. SENSITIVITY ANALYSIS ON VSC-HVDC SYSTEM CAPACITY

The cases with different HVDC system capacities are discussed in Table 3. The active power output of the wind power plant is 600MW. The frequency stability constraint f_{range} is fixed to be 0.12Hz. H_{vsc} value of the IEC control is zero.

In Table 3, the 'Active power' row shows the active power transmission via the HVDC system. The ratio of this active power transmission to the HVDC system capacity is denoted as the 'P ratio'. The 'Reserve capacity' indicates the available reserve capacity of the HVDC system. 'R ratio' corresponds to the ratio of this reserve capacity to the total HVDC system capacity. If the reserve capacity of the HVDC system is zero, the frequency support cannot be obtained due to the upper limit constraint of the VSC output power.

First of all, it is revealed that the 300MVA HVDC system is not sufficient for transmitting active power and securing the reserve capacity. On the other hand, the OPF solution can be found if the frequency stability constraint is larger than 0.12Hz in the preliminary simulation. The insufficient reserve

TABLE 3. Deload ratio of wind power plant R_{WT} with different HVDC system capacities.

	HVDC capacity (MVA)				
	300	400	500	600	1000
Active power (MW)	X	336	335	417	396
P ratio	X	0.839	0.670	0.696	0.396
Reserve capacity (MW)	X	64	165	183	604
R ratio	X	0.161	0.330	0.304	0.604
R_{WT}	X	0.954	0.954	0.986	0.997

capacity of the HVDC system is the most critical factor which determines the feasibility of the solution.

Feasible solutions can be calculated when the HVDC system capacity is at least 400MVA. The amount of active power transmission by the HVDC system is 335∼417MW. It should be noted that when the HVDC system capacity increases, the P ratio decreases and the R ratio increases overall. The HVDC system should have sufficient capacity for active power transmission. However, this transmission does not necessarily increase proportionally to the HVDC capacity above a certain value. The remaining capacity can be utilized as the reserve capacity for the primary frequency support. Owing to this reserve capacity, the necessity of the wind power deload operation can be reduced. Therefore, the lowest wind deload ratio can be obtained with the 1000MVA HVDC system.

VII. CONCLUSION

The impact of the primary frequency support of the VSC-HVDC systems on the wind power deload ratio is investigated. A frequency stability constrained OPF analysis for the hybrid AC/VSC-HVDC system models is formulated. The optimal wind output deload ratio can be determined by the FSC-OPF analysis. Inertia emulation control of the slack VSC converter can be implemented for the primary frequency support of VSC-HVDC systems. It is validated that the output curtailment of wind power plants is required to secure the reserve capacity and satisfy the frequency stability constraints. In contrast, the wind output suppression can be

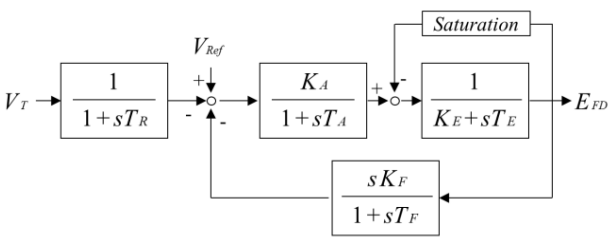

FIGURE 8. IEEE Type 1 excitation model [46].

reduced or avoided when the system frequency is supported by the inertia emulation control of a VSC-HVDC system.

In the future, the effect of the reactive power regulation by wind power plants will be assessed. Instead of the concentrated inertia emulation control method by the VSC slack converter, distributed frequency control methods by multi-terminal HVDC systems will be applied for future applications. The validity of the methodology will be discussed in different power system models and disturbance types. In addition, other stability issues such as rotor-angle and voltage stability constraints can be incorporated into the OPF formulation in future works.

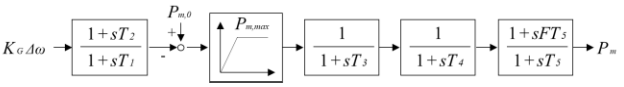

FIGURE 9. Turbine-governor model [47].

TABLE 4. AVR parameters of IEEE 39-Bus system.

	T_R (s)	K_A	T_A (s)	K_E	T_E (s)	K_F	T_F (s)
G1	1	200	0.358	1	0.004	0.0529	1
G2	1	400	0.0200	1	0.942	0.0300	1
G3	1	400	0.0200	1	0.942	0.0300	1
G4	1	400	0.0200	1	0.942	0.0300	1
G5	1	400	0.0200	1	0.942	0.0300	1
G6	1	400	0.0200	1	0.942	0.0300	1
G7	1	400	0.0200	1	0.942	0.0300	1
G8	1	400	0.0200	1	0.942	0.0300	1
G9	1	50	0.0600	-0.0393	0.440	0.0700	1

TABLE 5. Turbine-governor parameters of IEEE 39-Bus system.

	K_G	T_1 (s)	T_2 (s)	T_3 (s)	T_4 (s)	T_5 (s)	F
G1	20	0.2	0.4	0.3	0	10	0.3
G2	20	0.2	0.4	0.3	0	10	0.3
G3	20	0.2	0.4	0.3	0	10	0.3
G4	20	0.2	0.4	0.3	0	10	0.3
G5	20	0.2	0.4	0.3	0	10	0.3
G6	20	0.2	0.4	0.3	0	10	0.3
G7	20	0.2	0.4	0.3	0	10	0.3
G8	20	0.2	0.4	0.3	0	10	0.3
G9	20	0.2	0.4	0.3	0	10	0.3

TABLE 6. VSC-HVDC control system parameters.

System	Item	Value [$p.u.$]
PI Controller	Outer active power controller ($k_{p,p}$, $k_{i,p}$)	(1, 2)
	Outer reactive power controller ($k_{p,q}$, $k_{i,q}$)	(1, 2)
	Outer DC voltage controller ($k_{p,dc}$, $k_{i,dc}$)	(10, 20)
	Inner current controller (k_{pi}, k_{ii})	(1, 20)

APPENDIX

See Figures 8, 9, and Tables 4–6.

REFERENCES

[1] L. Xu, L. Yao, and C. Sasse, "Grid integration of large DFIG-based wind farms using VSC transmission," *IEEE Trans. Power Syst.*, vol. 22, no. 3, pp. 976–984, Aug. 2007.

[2] E. Pierri, O. Binder, N. G. A. Hemdan, and M. Kurrat, "Challenges and opportunities for a European HVDC grid," *Renew. Sustain. Energy Rev.*, vol. 70, pp. 427–456, Apr. 2017.

[3] J. Liu, W. Yao, J. Wen, J. Fang, L. Jiang, H. He, and S. Cheng, "Impact of power grid strength and PLL parameters on stability of grid-connected DFIG wind farm," *IEEE Trans. Sustain. Energy*, vol. 11, no. 1, pp. 545–557, Jan. 2020.

[4] Y. Li, G. Tang, T. An, H. Pang, P. Wang, J. Yang, Y. Wu, and Z. He, "Power compensation control for interconnection of weak power systems by VSC-HVDC," *IEEE Trans. Power Del.*, vol. 32, no. 4, pp. 1964–1974, Aug. 2017.

[5] G.-S. Lee, D.-H. Kwon, Y.-K. Kim, and S.-I. Moon, "A new communication-free grid frequency and AC voltage control of hybrid LCC-VSC-HVDC systems for offshore wind farm integration," *IEEE Trans. Power Syst.*, vol. 38, no. 2, pp. 1309–1321, Mar. 2023.

[6] Y. Zhang and A. M. Gole, "Quantifying the contribution of dynamic reactive power compensators on system strength at LCC-HVdc converter terminals," *IEEE Trans. Power Del.*, vol. 37, no. 1, pp. 449–457, Feb. 2022.

[7] H. Liu and Z. Chen, "Contribution of VSC-HVDC to frequency regulation of power systems with offshore wind generation," *IEEE Trans. Energy Convers.*, vol. 30, no. 3, pp. 918–926, Sep. 2015.

[8] Y. Xiong, W. Yao, J. Wen, S. Lin, X. Ai, J. Fang, J. Wen, and S. Cheng, "Two-level combined control scheme of VSC-MTDC integrated offshore wind farms for onshore system frequency support," *IEEE Trans. Power Syst.*, vol. 36, no. 1, pp. 781–792, Jan. 2021.

[9] Y. Wang, N. Zhang, C. Kang, M. Miao, R. Shi, and Q. Xia, "An efficient approach to power system uncertainty analysis with high-dimensional dependencies," *IEEE Trans. Power Syst.*, vol. 33, no. 3, pp. 2984–2994, May 2018.

[10] J. Li, S. Wang, L. Ye, and J. Fang, "A coordinated dispatch method with pumped-storage and battery-storage for compensating the variation of wind power," *Protection Control Modern Power Syst.*, vol. 3, no. 1, pp. 21–34, Dec. 2018.

[11] J. Zhu, C. D. Booth, G. P. Adam, A. J. Roscoe, and C. G. Bright, "Inertia emulation control strategy for VSC-HVDC transmission systems," *IEEE Trans. Power Syst.*, vol. 28, no. 2, pp. 1277–1287, May 2013.

[12] O. D. Adeuyi, M. Cheah-Mane, J. Liang, and N. Jenkins, "Fast frequency response from offshore multiterminal VSC–HVDC schemes," *IEEE Trans. Power Del.*, vol. 32, no. 6, pp. 2442–2452, Dec. 2017.

[13] L. Fan, Z. Miao, and D. Osborn, "Wind farms with HVDC delivery in load frequency control," *IEEE Trans. Power Syst.*, vol. 24, no. 4, pp. 1894–1895, Nov. 2009.

[14] Y. Phulpin, "Communication-free inertia and frequency control for wind generators connected by an HVDC-link," *IEEE Trans. Power Syst.*, vol. 27, no. 2, pp. 1136–1137, May 2012.

[15] M. M. Kabsha and Z. H. Rather, "A new control scheme for fast frequency support from HVDC connected offshore wind farm in low-inertia system," *IEEE Trans. Sustain. Energy*, vol. 11, no. 3, pp. 1829–1837, Jul. 2020.

[16] G.-S. Lee, D.-H. Kwon, S.-I. Moon, and P.-I. Hwang, "A coordinated control strategy for LCC HVDC systems for frequency support with suppression of AC voltage fluctuations," *IEEE Trans. Power Syst.*, vol. 35, no. 4, pp. 2804–2815, Jul. 2020.

[17] D. Yang, J. Kim, Y. C. Kang, E. Muljadi, N. Zhang, J. Hong, S.-H. Song, and T. Zheng, "Temporary frequency support of a DFIG for high wind power penetration," *IEEE Trans. Power Syst.*, vol. 33, no. 3, pp. 3428–3437, May 2018.

[18] M. Sun, Y. Sun, L. Chen, Z. Zou, Y. Min, R. Liu, F. Xu, and Y. Wu, "Novel temporary frequency support control strategy of wind turbine generator considering coordination with synchronous generator," *IEEE Trans. Sustain. Energy*, vol. 13, no. 2, pp. 1011–1020, Apr. 2022.

[19] Z. Chu, U. Markovic, G. Hug, and F. Teng, "Towards optimal system scheduling with synthetic inertia provision from wind turbines," *IEEE Trans. Power Syst.*, vol. 35, no. 5, pp. 4056–4066, Sep. 2020.

[20] M. Mehrabankhomartash, M. Saeedifard, and A. Yazdani, "Adjustable wind farm frequency support through multi-terminal HVDC grids," *IEEE Trans. Sustain. Energy*, vol. 12, no. 2, pp. 1461–1472, Apr. 2021.
[21] Y. Li, Z. Zhang, Y. Yang, Y. Li, H. Chen, and Z. Xu, "Coordinated control of wind farm and VSC–HVDC system using capacitor energy and kinetic energy to improve inertia level of power systems," *Int. J. Electr. Power Energy Syst.*, vol. 59, pp. 79–92, Jul. 2014.
[22] A. Junyent-Ferre, Y. Pipelzadeh, and T. C. Green, "Blending HVDC-link energy storage and offshore wind turbine inertia for fast frequency response," *IEEE Trans. Sustain. Energy*, vol. 6, no. 3, pp. 1059–1066, Jul. 2015.
[23] B. K. Poolla, D. Groß, and F. Dörfler, "Placement and implementation of grid-forming and grid-following virtual inertia and fast frequency response," *IEEE Trans. Power Syst.*, vol. 34, no. 4, pp. 3035–3046, Jul. 2019.
[24] C. Yang, L. Huang, H. Xin, and P. Ju, "Placing grid-forming converters to enhance small signal stability of PLL-integrated power systems," *IEEE Trans. Power Syst.*, vol. 36, no. 4, pp. 3563–3573, Jul. 2021.
[25] F. Zhao, X. Wang, Z. Zhou, L. Harnefors, J. R. Svensson, L. H. Kocewiak, and M. P. S. Gryning, "Control interaction modeling and analysis of grid-forming battery energy storage system for offshore wind power plant," *IEEE Trans. Power Syst.*, vol. 37, no. 1, pp. 497–507, Jan. 2022.
[26] J. D. Watson, Y. Ojo, K. Laib, and I. Lestas, "A scalable control design for grid-forming inverters in microgrids," *IEEE Trans. Smart Grid*, vol. 12, no. 6, pp. 4726–4739, Nov. 2021.
[27] L. Huang, H. Xin, and Z. Wang, "Damping low-frequency oscillations through VSC-HVdc stations operated as virtual synchronous machines," *IEEE Trans. Power Electron.*, vol. 34, no. 6, pp. 5803–5818, Jun. 2019.
[28] Y. Cao, W. Wang, Y. Li, Y. Tan, C. Chen, L. He, U. Häger, and C. Rehtanz, "A virtual synchronous generator control strategy for VSC-MTDC systems," *IEEE Trans. Energy Convers.*, vol. 33, no. 2, pp. 750–761, Jun. 2018.
[29] A. Asrari, M. Mustafa, M. Ansari, and J. Khazaei, "Impedance analysis of virtual synchronous generator-based vector controlled converters for weak AC grid integration," *IEEE Trans. Sustain. Energy*, vol. 10, no. 3, pp. 1481–1490, Jul. 2019.
[30] Q.-C. Zhong and G. Weiss, "Synchronverters: Inverters that mimic synchronous generators," *IEEE Trans. Ind. Electron.*, vol. 58, no. 4, pp. 1259–1267, Apr. 2011.
[31] H. Bevrani, T. Ise, and Y. Miura, "Virtual synchronous generators: A survey and new perspectives," *Int. J. Electr. Power Energy Syst.*, vol. 54, pp. 244–254, Jan. 2014.
[32] S. D'Arco and J. A. Suul, "Virtual synchronous machines—Classification of implementations and analysis of equivalence to droop controllers for microgrids," in *Proc. IEEE Grenoble Conf.*, Jun. 2013, pp. 1–7.
[33] A. Tayyebi, Z. Miletic, F. Dorfler, F. Kupzog, and W. Hribernik, "Grid-forming converters—Inevitability, control strategies and challenges in future grid applications," in *Proc. Int. Conf. Electr. Distrib. (CIRED)*, Ljubljana, Slovenia, 2018.
[34] V. Karapanos, S. de Haan, and K. Zwetsloot, "Real time simulation of a power system with VSG hardware in the loop," in *Proc. IECON 37th Annu. Conf. IEEE Ind. Electron. Soc.*, Nov. 2011, pp. 3748–3754.
[35] M. Torres and L. A. C. Lopes, "Virtual synchronous generator: A control strategy to improve dynamic frequency control in autonomous power systems," *Energy Power Eng.*, vol. 5, no. 2A, pp. 32–38, 2013.
[36] Z. Shen, J. Zhu, L. Ge, S. Bu, J. Zhao, C. Y. Chung, X. Li, and C. Wang, "Variable-inertia emulation control scheme for VSC-HVDC transmission systems," *IEEE Trans. Power Syst.*, vol. 37, no. 1, pp. 629–639, Jan. 2022.
[37] S. Kim, A. Yokoyama, Y. Takaguchi, T. Takano, K. Mori, and Y. Izui, "Transient stability constrained optimal power flow in mixed AC/multi-terminal VSC HVDC system," *IEEJ Trans. Electr. Electron. Eng.*, vol. 15, no. 10, pp. 1436–1447, Oct. 2020.
[38] S. Kim, "A novel preventive frequency stability constrained OPF considering wind power fluctuation," in *Proc. IEEE PES Innov. Smart Grid Technol. Asia (ISGT Asia)*, Nov. 2022, pp. 96–100.
[39] H. Saad, J. Peralta, S. Dennetière, J. Mahseredjian, J. Jatskevich, J. A. Martinez, A. Davoudi, M. Saeedifard, V. Sood, X. Wang, J. Cano, and A. Mehrizi-Sani, "Dynamic averaged and simplified models for MMC-based HVDC transmission systems," *IEEE Trans. Power Del.*, vol. 28, no. 3, pp. 1723–1730, Jul. 2013.
[40] J. Xu, A. M. Gole, and C. Zhao, "The use of averaged-value model of modular multilevel converter in DC grid," *IEEE Trans. Power Del.*, vol. 30, no. 2, pp. 519–528, Apr. 2015.
[41] X. Zhang, Y. Chen, Y. Wang, X. Zha, S. Yue, X. Cheng, and L. Gao, "Deloading power coordinated distribution method for frequency regulation by wind farms considering wind speed differences," *IEEE Access*, vol. 7, pp. 122573–122582, 2019.
[42] H. Luo, Z. Hu, H. Zhang, and H. Chen, "Coordinated active power control strategy for deloaded wind turbines to improve regulation performance in AGC," *IEEE Trans. Power Syst.*, vol. 34, no. 1, pp. 98–108, Jan. 2019.
[43] C. Li, Y. Wu, Y. Sun, H. Zhang, Y. Liu, Y. Liu, and V. Terzija, "Continuous under-frequency load shedding scheme for power system adaptive frequency control," *IEEE Trans. Power Syst.*, vol. 35, no. 2, pp. 950–961, Mar. 2020.
[44] A. Ademola-Idowu and B. Zhang, "Frequency stability using MPC-based inverter power control in low-inertia power systems," *IEEE Trans. Power Syst.*, vol. 36, no. 2, pp. 1628–1637, Mar. 2021.
[45] T. B. Nguyen and M. A. Pai, "Dynamic security-constrained rescheduling of power systems using trajectory sensitivities," *IEEE Trans. Power Syst.*, vol. 18, no. 2, pp. 848–854, May 2003.
[46] P. Demetriou, M. Asprou, J. Quiros-Tortos, and E. Kyriakides, "Dynamic IEEE test systems for transient analysis," *IEEE Syst. J.*, vol. 11, no. 4, pp. 2108–2117, Dec. 2017.
[47] X. Zhao, H. Wei, J. Qi, P. Li, and X. Bai, "Frequency stability constrained optimal power flow incorporating differential algebraic equations of governor dynamics," *IEEE Trans. Power Syst.*, vol. 36, no. 3, pp. 1666–1676, May 2021.
[48] C.-H. Lin and Y.-K. Wu, "Overview of frequency-control technologies for a VSC-HVDC-Integrated wind farm," *IEEE Access*, vol. 9, pp. 112893–112921, 2021.

SANGWON KIM (Member, IEEE) received the B.E. degree in electronic and electrical engineering from Sungkyunkwan University, Suwon, Republic of Korea, in 2015, and the M.E. and Dr.Eng. degrees in electrical engineering and information systems from The University of Tokyo, Japan, in 2017 and 2020, respectively. He was a Staff Engineer with the Global Manufacturing and Infrastructure Department, Samsung Electronics, South Korea, from 2020 to 2022. He is currently an Assistant Professor with the University of Ulsan, Ulsan, South Korea. His current research interests include power system operation and stability analysis, including HVDC systems and renewable energy integration.